# Multiharmonic Force Vector Model for Bearingless Electric Motors

Anvar Khamitov\* *Member, IEEE*, Eric L. Severson<sup>†</sup> *Senior Member, IEEE*\*Department of Electrical and Computer Engineering, University of Wisconsin-Madison, Madison, WI, USA

†Department of Mechanical Engineering, University of Minnesota, Minneapolis, MN, USA

Abstract—This paper proposes and develops a new analytic bearingless machine model that incorporates multiple airgap harmonic field interactions and has several advantages. The model can be used to address levitation performance requirements by developing force/torque regulation methods to precisely calculate commands to current regulators. This allows relaxing constraints during the design stage and has the potential to enable consideration of higher performance bearingless machines. Furthermore, analogous to torque enhancement in conventional electric machines, the proposed model can be used to identify options for suspension force enhancement in bearingless motors by controlling multiple magnetic field harmonics. This paper provides a detailed derivation of the model and shows how it can be used to improve force regulation accuracy and enhance force capacity. The paper finds that by controlling four airgap harmonic fields, instead of the typical two harmonics, force capacity can be increased by approximately 40%. Hardware measurements using a 10-phase bearingless induction machine validate the proposed model and force capacity increase.

Index Terms—Bearingless drive, bearingless motor, generalized Clarke transformation, multiphase winding, self-bearing motor

# I. INTRODUCTION

Bearingless motors have the potential to replace conventional motors with contact bearings and provide contact-free and lubricant-free support of the motor shaft [1]. However, their usage has been significantly limited by issues of low power density, efficiency, and high cost. Most bearingless motor prototypes reported in literature have been designed for low power ratings and relatively few machines have experimentally tested efficiencies of above 90% [2]-[4]. Furthermore, they are not achieving the speed-power capabilities of high performance conventional motors [2] nor the force capacity of active magnetic bearings [1]. All these limitations are because the design space of bearingless machines is significantly more constrained than conventional machines due to stringent levitation performance requirements. State-of-theart models and force regulation algorithms are based on the assumption of a linear force/torque-current relationship that ignores the effects of multiple airgap magnetic field harmonics and the possibility of using these unmodeled harmonics for reducing force ripple or increasing force capacity. As a result, potentially high performance designs that do not fall under these simplified model assumptions can be excluded from consideration during design studies.

This paper addresses the problem by proposing and developing a multiharmonic electric machine model that provides a new way of understanding force and torque creation. The new force vector terms included in the model account for

This work was supported in part by the USA National Science Foundation under Grant #1942099.

force generation in both separate and combined windings and are applicable to systems with any number of phases. The proposed model is based on current space vectors to allow identification of current sequence components that excite specific magnetic field harmonics to increase force capacity. The paper shows how the proposed model enables the creation of force/torque regulation techniques that can precisely actuate the shaft even when multiple airgap field harmonics are present. This allows relaxing the force vector error requirement during the design stage and addressing it during the control stage. As a result, this makes the design space less constrained and enables consideration of potentially higher performance designs. To the best of the authors' knowledge, only two studies, [5] and [6], have investigated techniques for precise force vector regulation. They demonstrated significant performance improvement for an active magnetic bearing (AMB) and a bearingless motor. Two other studies [3] and [7] made use of multiple space vector frames to develop the models for multisector and magnetically levitated rotary-linear machines. However, the techniques they developed only work for specific machine examples and no generalized analytic model was presented.

The main contribution of this paper is to propose, develop, and validate a new multiharmonic electric machine model that encompasses both force and torque creation, incorporating multiple airgap harmonic field interactions. Section II reviews airgap field theory that will be used in the model derivation. Sections III and IV review the textbook bearingless machine model typically used in literature, propose the multiharmonic model, and provide a detailed derivation from first principles using winding function theory, current sequences, and the Maxwell Stress Tensor. Section V demonstrate benefits of using the proposed model for force capacity enhancement. Section VI provides validation of the developed theory using hardware measurements from a 10-phase bearingless induction motor prototype. A conference version of this paper was published in [8], which showed that the prior models in [5] and [6] are special cases of the proposed model and demonstrated benefits of using the proposed model for force ripple minimization. This paper extends [8] with finite element analysis (FEA) and experiment results, which validate the proposed model and its potential benefits for force enhancement.

#### II. REVIEW OF AIRGAP FIELD THEORY

This section reviews the airgap field creation in bearingless electric machines as a special case of a more generalized multi-harmonic winding design study presented in [9]. The results

summarized in (12)-(15) and (18) are used in Section IV to develop the multiharmonic model proposed by this paper. Sections II-A and II-B review magnetic field space harmonics using winding function theory and the relation to the current sequence components. Section II-C shows how to use the airgap fields to calculate the forces and torque using a reformulated form of the Maxwell Stress Tensor.

# A. Harmonic Airgap Fields

This subsection reviews airgap magnetic field harmonics created by rotor magnets and stator winding currents. Winding function theory and circumferential current density are used to determine expressions for the winding fields. Assumptions for the derivation include an infinite iron permeability, the omission of slotting effects, and a constant normal magnetic field along the radial direction. Fields are evaluated at the inner bore of the stator at radius  $r_{\rm si}$ .

The normal and tangential components of the airgap magnetic field (see Fig. 1a) are given by

$$B_{\rm n} = B_{\delta} + B_{\rm n,w}, \quad B_{\rm tan} = B_{\rm tan,w} \tag{1}$$

where  $B_{\delta}$  is the rotor magnetic field, and  $B_{\rm n,w}$  and  $B_{\rm tan,w}$  are the winding's magnetic field components. The rotor magnetic field at harmonic h can be expressed in terms of the airgap angle  $\alpha$  and the rotor angular position  $\theta$  (defined in Fig. 1a):

$$B_{\delta,h} = \hat{B}_{\delta,h} \cos(h[\alpha - \theta]) \tag{2}$$

where  $\hat{B}_{\delta,h=p} = \hat{B}_{\delta}$  is the magnetic loading, which is the amplitude of the magnetizing/d-axis field evaluated at p pole pairs [10, Ch. 6-7]. An example plot of  $B_{\delta,h}$  along the airgap is illustrated in Fig. 1b.

The winding magnetic field depends on the winding layout and the phase currents. At space harmonic h:

$$B_{\text{n,w},h}(\alpha) = \frac{\mu_0}{\delta_{\text{eff}}} \sum_{k=1}^{m} N_{k,h}(\alpha) i_k, \ B_{\text{tan,w},h}(\alpha) = -\frac{\mu_0}{r_{\text{si}}} \sum_{k=1}^{m} A_{c,k,h}(\alpha) i_k$$

$$(3)$$

where  $\delta_{\rm eff}$  is the effective airgap length,  $r_{\rm si}$  is the stator inner radius,  $i_k$  is the phase current in phase k, and  $N_{k,h}(\alpha)$  is the winding function [11] harmonic h of phase k.  $A_{c,k,h}(\alpha)$  is the circumferential current density normalized by  $i_k$ , where  $A_{c,k,h}(\alpha)i_k$  represents the distribution of surface current along the inner bore of the stator, typically in A/rad [10, Ch. 1, 7]. The winding function describes the distribution of the per ampere magnetomotive force:

$$N_{k,h}(\alpha) = \hat{N}_h \cos(h\alpha - \alpha_{w0,h} - [k-1]h\alpha_{ph,w})$$
 (4)

where  $\hat{N}_h = \frac{2}{\pi h} z_Q z_c \hat{k}_{w,h}$  and  $\alpha_{\text{w0},h}$  are the winding function amplitude and phase shift at harmonic h.  $\hat{N}_h$  is determined by the number of turns per coil  $z_Q$ , coils per phase  $z_c$ , and the winding factor  $\hat{k}_{w,h}$ . The angle  $\alpha_{\text{ph,w}} = \frac{2\pi}{ms_\Theta}$  is the mechanical phase separation between adjacent phases, where  $s_\Theta$  is introduced in [9] to develop a generalized winding design theory to independently create multiple airgap harmonics. The value of  $s_\Theta$  can be any common divisor (CD) of the space harmonic orders  $\{h_1,h_2,...\}$  that the winding needs to create [9]. In separated windings, the value of  $s_\Theta$  is typically p and

 $p_s$  for torque and suspension windings, respectively. However, in combined windings,  $s_{\Theta} = \text{CD}(p, p_s) = 1$  [12].

Using the winding function, the normalized circumferential current density  $A_{c,k,h}(\alpha)$  (in 3) at harmonic h can be calculated based on the linear current density and the winding distribution [10, Ch. 7]:

$$A_{c,k,h}(\alpha) = -\frac{\mathrm{d}N_{k,h}(\alpha)}{\mathrm{d}\alpha} = A'_{c,\mathsf{ph},h} \sin\left(h\alpha - \alpha_{\mathsf{w0},h} - [k-1]h\frac{2\pi}{m}\right) \tag{5}$$

where  $A'_{c,ph,h} = h\hat{N}_h = \frac{2}{\pi}z_Qz_c\hat{k}_{w,h}$ . Substituting (4) and (5) into (3), the winding magnetic field components become:

$$B_{\text{n,w,}h}(\alpha) = \frac{\mu_0 \hat{N}_h}{\delta_{\text{eff}}} \sum_{k=1}^m i_k \cos\left(h\alpha - \alpha_{\text{w0,}h} - [k-1]h\frac{2\pi}{m}\right)$$

$$B_{\text{tan,w,}h}(\alpha) = -\frac{\mu_0 h\hat{N}_h}{r_{\text{si}}} \sum_{k=1}^m i_k \sin\left(h\alpha - \alpha_{\text{w0,}h} - [k-1]h\frac{2\pi}{m}\right)$$
(6)

The phase currents  $i_k$  in (6) determine the behavior of the winding magnetic field at harmonic h when summed over all phases, resulting in counterclockwise (CCW) rotating, clockwise (CW) rotating, oscillating, or zero field. The following subsection provides more details about this relationship.

#### B. Field Relation to Sequence Currents

This subsection reviews the relation between the airgap fields and the phase currents. Current sequence and space vector components are defined and used to determine the field harmonics that they create in the airgap.

Any set of multiphase currents  $i = \begin{bmatrix} i_1 & i_2 & ... & i_m \end{bmatrix}^T$  can be decomposed into current sequence components as

$$i = i_0 + i_1 + \dots + i_s + \dots + i_{s_m} = \sum_{s=0}^{s_m} i_s$$
 (7)

where each term on the right-hand side is a column matrix that represents a sequence of order s and has the form  $i_s = \begin{bmatrix} i_{s,1} & i_{s,2} & \dots & i_{s,m} \end{bmatrix}^T$ . The current at positive sequence s and phase order k is defined as

$$i_{s,k} = \hat{I}_s \cos\left(\phi_s - [k-1]s\frac{2\pi}{m}\right) \tag{8}$$

where each sequence s has an amplitude  $\hat{I}_s$ , a phase angle  $\phi_s$ , and a phase separation  $s^{2\pi}_m$ . The values of s can be

$$s = 0, 1, ..., s_{\text{m}}, \text{ where } s_{\text{m}} = \begin{cases} \frac{m-1}{2} \text{ for odd } m\\ \frac{m}{2} \text{ for even } m \end{cases}$$
 (9)

This set of positive sequences sequences fully defines the m-phase system as there are m independent variables. This includes the magnitudes of sequences s=0 and s=m/2 (for even m), and the magnitudes and angles of sequences 0 < s < m/2. Each sequence could alternatively be represented using a negative sequence instead. This corresponds to a change in the phase order, having  $-s\frac{2\pi}{m}$  in (8) instead of  $s\frac{2\pi}{m}$ . In electric machines, using either  $s\frac{2\pi}{m}$  or  $-s\frac{2\pi}{m}$  creates the same harmonic field content, but the direction of rotation (CCW or CW) of these harmonics is reversed.

The current sequences can be decoupled from each other by applying the Generalized Clarke Transform (GCT) [13], [14]. As a result, each sequence component has an independent complex space vector representation in the stationary frame. The space vector  $\vec{i}_s$  for sequence s is found as

$$\vec{i}_s = C_m \sum_{k=1}^m e^{js(k-1)2\pi/m} i_k \tag{10}$$

where  $C_m$  is the transformation coefficient. Using this equation with  $C_m=2/m$ , it can be shown that space vectors for the sequences s=0 and s=m/2 have 1-DOF (only real part) and a form of  $\vec{i}_s=2\hat{I}_s\cos\phi_s$ . Space vectors for all other sequences have 2-DOF (real and imaginary parts) and a form of  $\vec{i}_s=\hat{I}_se^{j\phi_s}$ . This space vector representation of each sequence can be conveniently used to describe the magnetic field and force/torque creation.

Substituting (8) into (6) allows determining the magnetic field harmonics that are created due to a current sequence s (assuming that a winding factor  $\hat{k}_{w,h} \neq 0$  at each harmonic). The terms inside the summation in (6) have the form of  $\cos\left(\phi_s - [k-1]s\frac{2\pi}{m}\right)\cos\left(h\alpha - [k-1]h\frac{2\pi}{m}\right)$ . For any values of s, h, and m, the summation in (6) is non-zero only if the phase separation angles  $h\frac{2\pi}{m}$  and  $s\frac{2\pi}{m}$  are equal:

$$h\frac{2\pi}{m} = \pm s\frac{2\pi}{m} + 2\pi b \tag{11}$$

where  $2\pi b$  (b is an integer) indicates periodicity. Simplifying this equation shows that the sequence s can create the following airgap field harmonics:

$$h = \begin{cases} s + mb, & \text{for CCW rotating fields} \\ -s + mb, & \text{for CW rotating fields} \end{cases}$$
 (12)

and the total magnetic field expression at these harmonics is

$$B_{n,w,h}(\alpha) = \hat{B}_{n,w,h} \cos(h\alpha - \phi_h)$$

$$B_{tan,w,h}(\alpha) = -\hat{B}_{tan,w,h} \sin(h\alpha - \phi_h)$$
(13)

where  $\phi_h=\pm\phi_s+\alpha_{\rm w0,h}$  is an angular location of a field harmonic h in electrical degrees. The + and - signs indicate CCW or CW rotation. For example, a sequence s=2 in m=5 can create harmonics at h=2,7,12,... rotating CCW and h=3,8,13,... rotating CW.

The magnetic field amplitudes in (13) are

$$\hat{B}_{\text{n,w,}h} = \frac{m}{2} \frac{\mu_0 \hat{N}_h \hat{I}_s}{\delta_{\text{off}}}, \ \hat{B}_{\text{tan,w,}h} = \frac{m}{2} \frac{\mu_0 h \hat{N}_h \hat{I}_s}{r_{\text{ci}}}$$
(14)

When s = 0 or s = m/2, the magnetic field harmonics have an oscillating behavior (no rotation):

$$B_{\text{n,w,h}} = \hat{B}_{\text{n,w,h}} \left[ \cos \left( h\alpha - \alpha_{\text{w0,h}} - \phi_s \right) + \cos \left( h\alpha - \alpha_{\text{w0,h}} + \phi_s \right) \right]$$

$$B_{\text{tan,w,h}} = \hat{B}_{\text{tan,w,h}} \left[ \sin \left( h\alpha - \alpha_{\text{w0,h}} - \phi_s \right) + \sin \left( h\alpha - \alpha_{\text{w0,h}} + \phi_s \right) \right]$$
(15)

Equations (12)-(14) show that the current sequence s ( $\hat{I}_s$  and  $\phi_s$ ) can be used to control the amplitude and angular location of the airgap magnetic field at harmonic h. Analogously, injecting multiple current sequences as in (7) allows controlling multiple airgap field harmonics. These results are used in the following section to develop the bearingless machine model.

#### C. Complex Representation of Force Vector

Force and torque creation in electric machines directly depend on the airgap magnetic fields and can be described by the Maxwell Stress Tensor. This paper reformulates the standard Maxwell Stress Tensor formula in vector form as (16), which facilitates the derivation of the proposed model:

$$\vec{F} = \frac{r_{\rm si}L}{2\mu_0} \int_0^{2\pi} e^{j\alpha} \left[ B_{\rm n} + j B_{\rm tan} \right]^2 {\rm d}\alpha, \ \tau = \frac{r_{\rm si}^2 L}{\mu_0} \int_0^{2\pi} B_{\rm n} B_{\rm tan} {\rm d}\alpha \tag{16}$$

where  $\vec{F} = F e^{j\phi} = F_x + j F_y$  is the force vector with magnitude F and angular direction  $\phi$  and  $\tau$  is the torque, as shown in Fig. 1c. L is the axial length,  $B_{\rm n}$  and  $B_{\rm tan}$  are the normal and tangential components of the airgap magnetic field, and  $\alpha$  is the airgap angle (see Fig. 1a).

It is well-known that torque is created from the interaction between field harmonics of the same order h, while forces are created from the interaction between adjacent harmonics h and  $h \pm 1$  [1]. This can be shown using (16). Suppose that the airgap field consists of two harmonics  $h_1$  and  $h_2 > h_1$ :

$$B_{n} = \hat{B}_{n,h_{1}}\cos(h_{1}\alpha - \phi_{h_{1}}) + \hat{B}_{n,h_{2}}\cos(h_{2}\alpha - \phi_{h_{2}})$$

$$B_{tan} = -\hat{B}_{tan,h_{1}}\sin(h_{1}\alpha - \phi_{h_{1}}) - \hat{B}_{tan,h_{2}}\sin(h_{2}\alpha - \phi_{h_{2}})$$
(17)

By substituting these field expressions into the force equation in (16) and using the relation  $\cos x = 0.5(e^{jx} + e^{-jx})$ , the integrand in (16) can be expressed as a sum of complex exponential terms. Among these terms, only the ones that do not depend on  $\alpha$  can result in non-zero integration. It can be shown that this condition is satisfied only when  $h_2 = h_1 + 1$ .

As a result, solving (16) results in the following force expression:

$$\vec{F}_{h_{12}} = \frac{V_r}{2\mu_0 r_{\rm si}} \left( \hat{B}_{{\rm n},h_1} - \hat{B}_{{\rm tan},h_1} \right) \left( \hat{B}_{{\rm n},h_2} + \hat{B}_{{\rm tan},h_2} \right) e^{j(\phi_{h_2} - \phi_{h_1})} \tag{18}$$

where  $V_r = \pi r_{\rm si}^2 L$ . Note that (18) is a general expression for force created by field harmonics  $h_1$  and  $h_2$ . These fields can be from windings, magnets, or saliency. When the fields are created from windings, it is possible and convenient to express (18) in terms of normal field quantities alone. This is done by using the relation  $\hat{B}_{\tan,h} = \frac{h\delta_{\rm eff}}{r_{\rm si}}\hat{B}_{\rm n,h}$ , from (14), in (18) to obtain

$$\vec{F}_{h_{12}} = \frac{V_r}{2\mu_0 r_{\rm si}} C_{h_{ij}} \hat{B}_{{\rm n},h_1} \hat{B}_{{\rm n},h_2} e^{j(\phi_{h_2} - \phi_{h_1})}$$
 (19)

where  $C_{h_{12}} = \left(1 - \frac{h_1 \delta_{\rm eff}}{r_{\rm si}}\right) \left(1 + \frac{h_2 \delta_{\rm eff}}{r_{\rm si}}\right)$  with  $h_2 = h_1 + 1$ . When  $h_{1/2} \delta_{\rm eff} \ll r_{\rm si}$ ,  $C_{h_{ij}} \approx 1$ . The results (18)-(19) are used in the following sections to first derive the traditional bearingless machine model (the "textbook" model) and then to derive the new electric machine model from the perspective of multiple airgap harmonic field interactions.

# III. TEXTBOOK MODEL

This section provides an overview of the bearingless machine textbook model, i.e. [1], used in literature. The derivation of the force/torque equations is accomplished using the field calculations presented in Section II and its impact on machine design will be discussed.

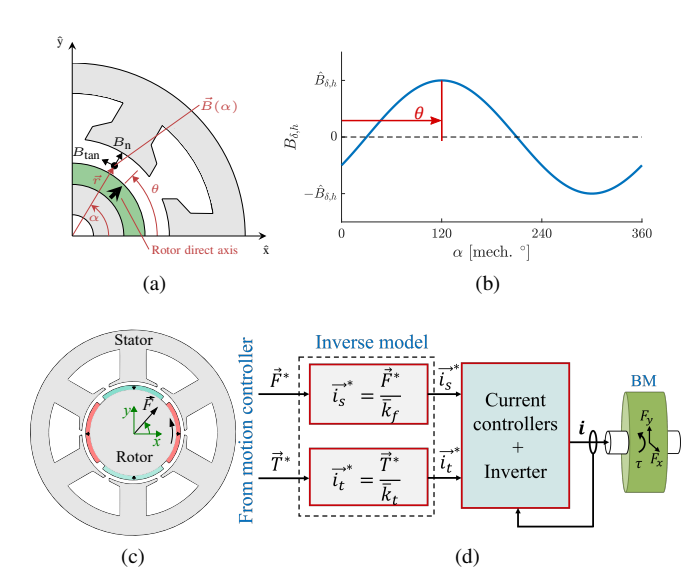


Fig. 1. (a) Magnetic field components and angles ( $\alpha$  and  $\theta$ ), (b) an example plot of the rotor magnetic field along the airgap at h=1, (c) force vector  $\vec{F}$  and torque  $\tau$ , and (d) force/torque regulation block diagram.

#### A. Force/torque calculations

The textbook model assumes that the airgap field consists of only p and  $p_s$  pole pairs. Considering the fields from the magnets (2) and the windings (3), the total airgap magnetic field components have the form (the phase shift angle  $\alpha_{\text{w0},p/p_s}$  is omitted for simplicity):

$$B_{n} = \hat{B}_{\delta} \cos(p[\alpha - \theta]) + \hat{B}_{n,w,p} \cos(p\alpha - \phi_{t}) + \hat{B}_{n,w,p_{s}} \cos(p_{s}\alpha - \phi_{s})$$
(20)  
$$B_{tan} = -\hat{B}_{tan,w,p} \sin(p\alpha - \phi_{t}) - \hat{B}_{tan,w,p_{s}} \sin(p_{s}\alpha - \phi_{s})$$

where the subscripts t and s denote the torque and suspension current sequences used to excite p and  $p_s$  pole pairs.

The force vector expression can be derived using (18). When  $h_1 = p$  or  $h_2 = p$  is created by the magnets,  $\hat{B}_{n,h_1/h_2} = \hat{B}_{\delta}$ ,  $\hat{B}_{\tan,h_1/h_2} = 0$ ,  $\phi_{h_1}/\phi_{h_2} = \theta_e = p\theta$ , and (18) simplifies to:

$$\vec{F} = \frac{V_r \hat{B}_{\delta}}{2\mu_0 r_{\rm si}} \left( \hat{B}_{\rm n,w,p_s} \pm \hat{B}_{\rm tan,w,p_s} \right) e^{\pm j(\phi_s - \theta_e)}$$

$$\tau = \frac{V_r}{\mu_0} \hat{B}_{\delta} \hat{B}_{\rm tan,w,p} \sin(\phi_t - \theta_e) \tag{21}$$

where the  $\pm$  signs correspond to  $p_s=p\pm 1$ . Substituting (14) into (21), the force/torque expressions can be expressed in terms of the suspension and torque current space vectors as

$$\vec{F} = \bar{k}_t \vec{i}_s, \quad \vec{T} = \bar{k}_t \vec{i}_t \tag{22}$$

where the flux weakening component  $T_d$  is included in  $\vec{T} = T_d + j\tau$ . Parameters  $\bar{k}_f$  and  $\bar{k}_t$  are the per ampere force and torque

$$\bar{k}_f = \frac{\hat{B}_{\delta} V_r m p_s \hat{N}_{p_s}}{4 r_{\rm si}} \left( \frac{1}{p_s \delta_{\rm eff}} \pm \frac{1}{r_{\rm si}} \right) e^{\mp j \theta_e}, \ \bar{k}_t = \frac{\hat{B}_{\delta} V_r m p \hat{N}_p}{2 r_{\rm si}} e^{-j \theta_e}$$
(23)

While  $\vec{i}_s$  and  $\vec{i}_t$  are calculated with the conventional CT for separated windings, [15] shows how this concept can be extended to multiphase (MP) and dual-purpose no voltage (DPNV) combined windings with the GCT.

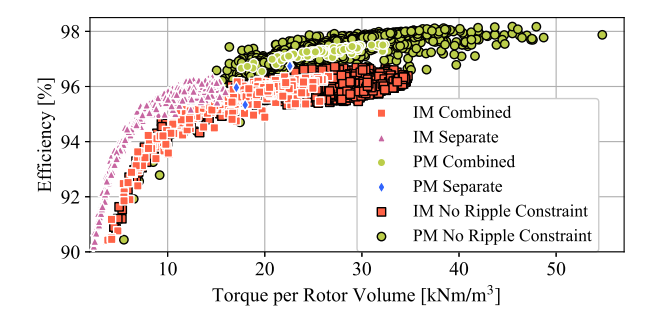


Fig. 2. Design study results for 100 kW and 30 kRPM replotted from [2, Section III-E].

#### B. Discussion

The textbook model (22) is based on dq control theory. The motor and suspension operation can be controlled in two independent space vector frames [14], [16] using the GCT and Park transformations. Desired phase currents are calculated by inverting the model (see Fig. 1d). The control algorithm introduced in [1, Ch. 7, 9] further accounts for the influence of armature reaction on suspension forces to mitigate angular shifts in force vector orientation caused by non-zero torque.

This model assumes perfectly sinusoidal airgap fields and its solution results in sinusoidal phase currents. The unmodeled magnetic field harmonics, armature reaction, and nonlinearities can cause large force vector error [1], [17]. The conference version of this paper [8, Fig. 2a] demonstrated fluctuations in the force vector over a rotor revolution due to unmodeled harmonics. This problem is typically solved in bearingless motor design studies by imposing the maximum error limits as constraints when sinusoidal phase currents are applied [18], [19]. However, this approach narrows the design space. Higher performance designs can be obtained if a more accurate machine model is used to determine the phase currents. Data from [2, Section III-E] has been replotted in Fig. 2 for permanent magnet (PM) and induction machines (IM) to demonstrate that 30% or more increase in torque density along with efficiency improvements up to 98% are possible when the force ripple constraint is removed.

#### IV. PROPOSED MULTIHARMONIC MODEL

This section proposes a new electric machine model that incorporates multiple airgap harmonic field interaction. This proposed model is the primary contribution of this paper. The model is applicable to all motor types, including PM, IM, and reluctance type motors. Section IV-A provides additional force calculations that are not considered in the textbook model (22). Based on this, Section IV-B proposes the generalized model for bearingless machines, discusses its properties, and provides examples for different number of phases.

#### A. Additional terms in force calculation

As was previously mentioned, the suspension forces are created from the interaction between adjacent magnetic field space harmonics h and  $h\pm 1$ . Based on this fact and (12)–(13),

this paper identifies two additional force creation mechanisms that are not considered in the textbook model:

- Forces from two adjacent current sequences. While this
  can include the interaction between torque and suspension current sequences (armature reaction<sup>1</sup>), it also
  includes interactions between other additional sequences
  that can be injected.
- 2) Forces from a single current sequence  $s_{\rm m}$  (only occurs in machines with an odd number of phases m).

These two force creation mechanisms are now discussed. Analogous to the derivation in Section III-A, the force vector expression derived in (18) is used.

1) Force from two adjacent current sequences: Force can be created by applying two adjacent current sequences  $s_1$  and  $s_2 = s_1 + 1$ , as (12) shows that this creates pairs of adjacent harmonics  $h_1$  and  $h_2 = h_1 + 1$  which rotate in the same direction (CCW or CW). The resulting airgap field and force are given by (17) and (18). Using (14), (18) can be expressed in terms of the current sequence components:

$$\vec{F}_{h_{12}} = \bar{k}_{h_{12}} \hat{I}_{s_1} \hat{I}_{s_2} e^{j(\phi_{h_2} - \phi_{h_1})} = \bar{k}_{h_{12}} \vec{i}_{s_1}^* \vec{i}_{s_2}$$

$$\bar{k}_{h_{12}} = \frac{\mu_0 V_r m^2 \hat{N}_{h_1} \hat{N}_{h_2}}{8r_{\rm si}^2} \left( \frac{r_{\rm si}}{\delta_{\rm eff}^2} - \frac{h_1 h_2}{r_{\rm si}} + \frac{1}{\delta_{\rm eff}} \right) e^{j(\alpha_{\rm w0,h_2} - \alpha_{\rm w0,h_1})}$$
(24)

2) Force from a single current sequence: Force can be created by injecting the highest current sequence  $s_{\rm m}=\frac{m-1}{2}$  in odd phase windings. Equation (12) shows that this creates pairs of adjacent harmonics that rotate in opposite directions: for every integer value of  $c \geq 0$ , harmonics exist at  $h_1 = s_{\rm m} + mc$  and  $h_2 = -s_{\rm m} + m(c+1)$ :

$$h_2 = -s_m + m(c+1) = -s_m + mc + m - 1 + 1$$
  
=  $-s_m + mc + 2s_m + 1 = h_1 + 1$  (25)

The created pairs of harmonics are  $(s_m, s_m + 1)$ ,  $(s_m + m, s_m + m + 1)$ ,  $(s_m + 2m, s_m + 2m + 1)$ , ...

Similar to Section IV-A1, the total airgap magnetic field and the force vector due to these adjacent harmonics can be described by (17) and (18). However, since these harmonics rotate in opposite directions and are created by the same sequence  $s_{\rm m}$ , their angular locations are  $\phi_{h_1} = \phi_{s_{\rm m}}$ ,  $\phi_{h_2} = -\phi_{s_{\rm m}}$  and their amplitudes depend on  $\hat{I}_{s_{\rm m}}$ , described by (14). This results in the following force expression:

$$\vec{F}_{h_{12}} = \bar{k}_{h_{12}} \hat{I}_{s_m}^2 e^{-j2\phi_{s_m}} = \bar{k}_{h_{12}} \vec{i}_{s_m}^{*2}$$
 (26)

This equation shows that the single sequence  $s_{\rm m}$  can be used to control the force vector magnitude  $F_{h_{12}}=\bar{k}_{h_{12}}\hat{I}_{s_{\rm m}}^2$  and angle  $\phi=-2\phi_{s_{\rm m}}$ .

The quadratic force vector component in (26) is not considered in other bearingless motor literature publications which is surprising given that this force also appears in bearingless machines with three-phase windings. This includes all three-phase combined windings where s=0 creates torque (if there is a zero-sequence current path) and s=1 creates force. For example, a three-phase motor with a concentrated winding, Q=6 slots, and p=3 and  $p_s=4$  pole pairs has these characteristics. This quadratic term also appears in all three-phase separated windings with  $s_{\Theta}=1$  (always true when

p=1 or  $p_s=1$ ). If these quadratic terms are not accounted for, conventional design processes attempt to minimize these terms (presumably through the use of large effective airgap lengths) as they create force vector error. Instead, if these new terms are handled in the force regulator, designers can enhance these terms to increase the suspension force capability.

Alternatively, if the designer desires to eliminate the effects of the quadratic term  $\bar{k}_{h_{12}} \vec{i}_s^{*2}$  (for example, in a five-phase bearingless motor), it can be shown using the equation for  $\bar{k}_{h_{12}}$  in (24) that this can be accomplished for a machine with  $p_s = p+1$  when the machine design parameters are selected to have the relation  $p_s \delta_{\rm eff} = r_{\rm si}$ . This can be advantageous for machines with a small rotor radius, high rated speed, and/or a high number of pole pairs.

## B. Generalized force model

The total force acting on the rotor due to all harmonics is now summarized in a single model. This is calculated as the vector sum of the force due to each pair of adjacent field harmonics  $h_i$  and  $h_j = h_i + 1$ :  $\vec{F} = \sum \vec{F}_{h_{ij}}$ , where each force vector component  $\vec{F}_{h_{ij}}$  is described by (18). Based on the force/torque derivations in Sections III-A and IV-A, three types of force components  $\vec{F}_{h_{ij}}$  are identified that differ by their dependence on current space vectors:

- Textbook model: force from stator-rotor harmonic interactions. This term has a linear dependence on the current space vector and is summarized in (22).
- New term 1: force from stator-stator harmonic interactions where each harmonic is created by a unique current sequence. This term depends on the product of two current space vectors, see (24).
- New term 2: force from stator-stator harmonic interactions where both harmonics are created by the same current sequence. This term depends on the square of a single current space vector (26).

This paper proposes a force model that compiles the force terms created by all current sequence components that can be injected into the m-phase winding.

1) Matrix representation: The proposed model is written in matrix form as

$$\vec{F} = \vec{i}^T \bar{T}_Q \vec{i} + \bar{T}_L \vec{i} + \vec{F}_C \tag{27}$$

where  $\vec{i}$  is an  $m \times 1$  array of the current space vectors and their conjugates calculated from the GCT matrix  $C_m$  as  $\vec{i} = C_m i$ :

$$\vec{i} = \begin{bmatrix} \vec{i}_0 & \vec{i}_1 & \vec{i}_2 & \dots & \vec{i}_2^* & \vec{i}_1^* \end{bmatrix}^T$$
 (28)

and  $\bar{T}_Q$  and  $\bar{T}_L$  are  $m \times m$  and  $1 \times m$  complex matrices that model the quadratic and linear dependencies of the force on the current space vectors, and  $\vec{F}_C$  is the cogging force.

Every entry of  $\bar{T}_Q$  is determined by (24) and represents the force per ampere squared created due to two current space vectors. This includes the forces due to two adjacent current space vectors as in (24)  $(\vec{i}_1^* \vec{i}_2, \vec{i}_2^* \vec{i}_3, ...)$  and due to the space vector  $s_m$  as in (26)  $(\vec{i}_{s_m}^{*2})$ . Every entry of  $\bar{T}_L$  is a force per ampere given in (23), which shows an interaction between adjacent rotor-stator field harmonics created by one current

<sup>&</sup>lt;sup>1</sup>Armature reaction is considered in the control algorithm of [1, Ch. 6].

space vector  $(\vec{i}_1, \vec{i}_2, ...)$ . Note that the  $\vec{i}_t$  and  $\vec{i}_s$  space vectors of the textbook model (22) are present in (28), but indicated as a sequence number; i.e.  $\vec{i}_t = \vec{i}_1$  and  $\vec{i}_s = \vec{i}_2$ .

The proposed model in (27) can incorporate multiple harmonics by adjusting  $\bar{T}_Q$  and  $\bar{T}_L$  matrix entries, allowing users to specify the number of harmonics based on their desired accuracy. Every entry of  $\bar{T}_Q$  is a sum of the terms in (24) as  $\bar{K}_{s_{ij}} = \sum \bar{k}_{h_{ij}}$  for all adjacent airgap harmonics  $h_i$  and  $h_j$  created by the sequences  $s_i$  and  $s_j = s_i + 1$  or the sequence  $s_m$  in odd phase machines. Similarly, every entry of  $\bar{T}_L$  is the sum of the terms in (23) as  $\bar{K}_{s_i} = \sum \bar{k}_{f,h_{ir}}$  for all adjacent harmonics  $h_i$  and  $h_r$  created by the sequence  $s_i$  and the rotor magnets. Depending on the relative rotation direction of these harmonics, some harmonic interactions result in a force ripple (having the  $e^{j\pm 2\theta}$  term) or a constant force.

2) Space vector representation: Since only specific entries of  $\overline{T}_Q$  are non-zero, the proposed model (27) can be rewritten using (22), (24), and (26) for even phase machines as:

$$\vec{F} = \sum_{i=1}^{s_{\rm m}-2} \bar{K}_{s_{ij}} \vec{i}_{s_i}^* \vec{i}_{s_j} + \sum_{i=1}^{s_{\rm m}-1} \left( \bar{K}_{s_i} \vec{i}_i + \bar{K}_{s_i^*} \vec{i}_{s_i}^* \right)$$
(29)

and for odd phase machines as,

$$\vec{F} = \bar{K}_{s_{m}s_{m}}\vec{i}_{s_{m}}^{*2} + \sum_{i=1}^{s_{m}-1} \bar{K}_{s_{ij}}\vec{i}_{s_{i}}^{*}\vec{i}_{s_{j}} + \sum_{i=1}^{s_{m}} \left(\bar{K}_{s_{i}}\vec{i}_{s_{i}} + \bar{K}_{s_{i}^{*}}\vec{i}_{s_{i}}^{*}\right)$$
(30)

where  $\vec{F}_C$  is omitted to save space. Note that odd phase machines have an additional term that depends on the space vector  $s_{\rm m}$  due to (26). The term  $\bar{K}_{s_i^*}\vec{i}_{s_i}^*$  is a force ripple term from interaction between adjacent magnet and winding field harmonics that rotate in opposite directions. Depending on the desired model accuracy, the coefficients in (29) and (30) can be modified to include the desired number of space harmonics.

3) Examples: To demonstrate the use of the proposed model, a force vector equation for an example nine-phase machine is now provided by expanding (30) (assuming that the rotor magnetic field is purely sinusoidal):

$$\vec{F}_{9\text{-ph}} = \bar{k}_{h_{45}} \vec{i}_{4}^{*2} + \bar{k}_{h_{34}} \vec{i}_{3}^{*} \vec{i}_{4} + \bar{k}_{h_{23}} \vec{i}_{2}^{*} \vec{i}_{3} + \bar{k}_{h_{12}} \vec{i}_{1}^{*} \vec{i}_{2} + \bar{k}_{f} \vec{i}_{s}$$
(31)

This machine has four independent rotating current space vectors. Here,  $\bar{k}_f \vec{i}_s$  is the force from stator-rotor interaction and  $\vec{i}_s$  can be any space vector between  $\vec{i}_1$  and  $\vec{i}_4$  depending on  $p_s$ . Coefficients  $\bar{k}_{h_{12}}$ ,  $\bar{k}_{h_{23}}$ ,  $\bar{k}_{h_{34}}$ ,  $\bar{k}_{h_{45}}$  are the entries of  $\bar{T}_Q$  and are calculated using (24). Differing from the textbook model (22), (31) shows that the proposed model has multiple quadratic terms. Accounting for these terms in a bearingless machine design study can potentially yield bearingless machine designs with enhanced force capability.

The proposed model (27) can be used to find the force vector expression for any m. As further examples, consider five- and six-phase machines, which have two rotating space vectors  $\vec{i}_1$  and  $\vec{i}_2$ . When  $\vec{i}_1 = \vec{i}_t$  and  $\vec{i}_2 = \vec{i}_s$ , force vector expressions can be obtained analogous to (31):

$$\vec{F}_{\text{5-ph}} = \bar{k}_q \vec{i}_s^{*2} + \bar{k}_{ft} \vec{i}_t^* \vec{i}_s + \bar{k}_f \vec{i}_s, \ \vec{F}_{\text{6-ph}} = \bar{k}_{ft} \vec{i}_t^* \vec{i}_s + \bar{k}_f \vec{i}_s \quad (32)$$

where  $\bar{k}_q$  and  $\bar{k}_{ft}$  are the entries of  $\bar{T}_Q$  matrix in (27). As in (31), these equations have new quadratic terms due to two

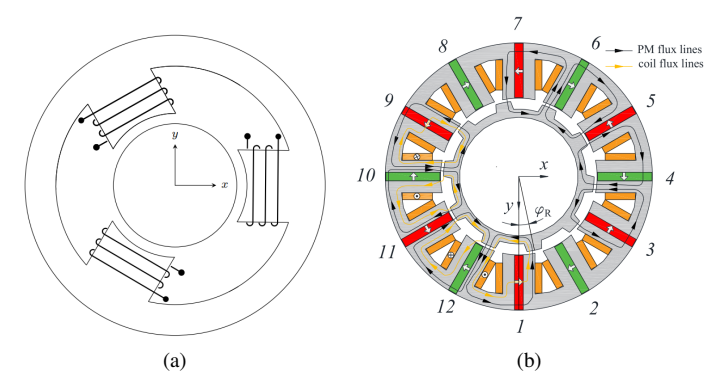


Fig. 3. Electric machine cross-sections used in the development of the models for precise force vector regulation in: (a) three-pole AMB in [5] and (b) bearingless flux-switching motor in [6].

adjacent space vectors  $\vec{i}_s^*\vec{i}_s$  and the highest space vector  $\vec{i}_s^{*2}$  for m=5. The  $\vec{i}_s^{*2}$  term also appears in bearingless machines with three phases, as was discussed in Section IV-A2. To avoid force vector error created by these quadratic terms, (32) can be used to implement precise force vector regulation by analytically solving for phase current commands that eliminate force vector error, as demonstrated in the conference version of this paper [8, Fig. 2a].

#### V. FORCE ENHANCEMENT

This section investigates how the proposed model can be used to enhance the force capacity of bearingless motors through control of multiple airgap harmonic fields. Bearingless machines with m=5 through 10 phases are compared in terms of their rated force capabilities, current requirements, ohmic losses, and simultaneous torque capability. The machines are compared over a range of magnetizing field  $B_{\delta}$ values as this is a critical design parameter in motor sizing. All examples have p = 1, the same motor dimensions, and the same total number of turns  $mz_Qz_c$  (same  $R_{ph}m$ , where  $R_{ph}$ is the phase winding resistance), where  $z_Q$  and  $z_c$  are defined in (4). The analysis considers only the desired harmonic per sequence, which is the same as the sequence number for these examples (refer to (12) with b = 0). The calculations assume unity winding factors for these harmonics to allow a comparison in per-unit [p.u.] quantities and identify the maximum potential of multiphase windings in creating and enhancing force capacity. Appendix A provides the p.u. force vector model (35) and the base values (36) used in this section.

#### A. Force Rating

First, the machines are compared in terms of their rated force capabilities. Using the definition of  $F_{\rm rated}$  (also known as the load capacity) in [20, Ch. 6], the dimensionless model (35) allows finding  $F_{\rm rated}$  as follows:

- 1) Solve for the field quantities to find the maximum force profile  $F'_{\max}(\phi)$  in all directions  $\phi$ , while satisfying  $\max(|B'_{\mathbf{n}}(\alpha)|) \leq 1$  (solved as an optimization problem in Matlab).
- 2) Find the rated force as  $F'_{\text{rated}} = \min [F'_{\text{max}}(\phi)]$ ; this is the force that can be guaranteed at all angles.

Using the result from these steps, force capacity/specific load capacity, defined as the load capacity per projected rotor area (diameter  $\times$  length) [20, Ch. 6], can be found as

$$f_c = \frac{F'_{\text{rated}} F_{\text{b}}}{DL} = \frac{\pi}{4\mu_0} B_{\text{max}}^2 F'_{\text{rated}}$$
 (33)

The results after following these steps are provided in Fig. 4a, which shows the maximum force profile and the rated force (shown as an inscribed red dashed circle for  $\hat{B}'_{\delta}=0.5$  p.u.). Based on this, the rated force vs.  $\hat{B}_{\delta}$  is obtained and plotted in Fig. 4b (top subplot). Figure 4a illustrates that, unlike other phases, the m=5 machine has non-convex maximum force profiles for a range of  $\hat{B}_{\delta}$  values. This results in  $F_{\rm rated}$  being a non-convex function of  $\hat{B}_{\delta}$ , as shown in Fig. 4b (two maxima at  $\hat{B}'_{\delta}=0$  and 0.7 p.u.). This is due to the quadratic term in (32), which also appears in certain three-phase separated windings and three-pole AMBs [5]. Figure 4b also compares the current rating and the average ohmic losses per unit of the rated force (subplots 2 and 3). The currents are calculated using the p.u. field quantities and the base value  $I_{\rm b}$ , as given in (36).

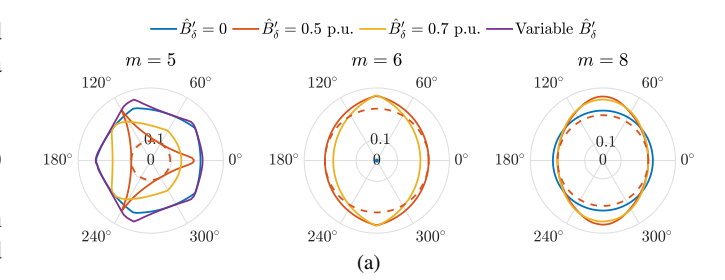
These results show that machines with  $m\geq 8$  phases can maintain their force capability over the widest range of  $\hat{B}_\delta$  values. For  $\hat{B}_\delta'\leq 0.2$  p.u., m=6 has the poorest performance (lowest force rating, highest current rating and ohmic losses). At  $\hat{B}_\delta'\approx 0$ , machines with m=5 have the lowest current rating and ohmic losses, while having the same force rating as other phases. This is because m=5 machines can use the sequence corresponding to the quadratic term in (32), s=2, to create suspension forces. The m=10 machine has the largest force rating, with the maxima occurring at  $\hat{B}_\delta'=0.5$  p.u., because it can independently control four harmonics, which adds more degrees of freedom to satisfy  $\max(|B_{\rm n}'(\alpha)|)\leq 1$ .

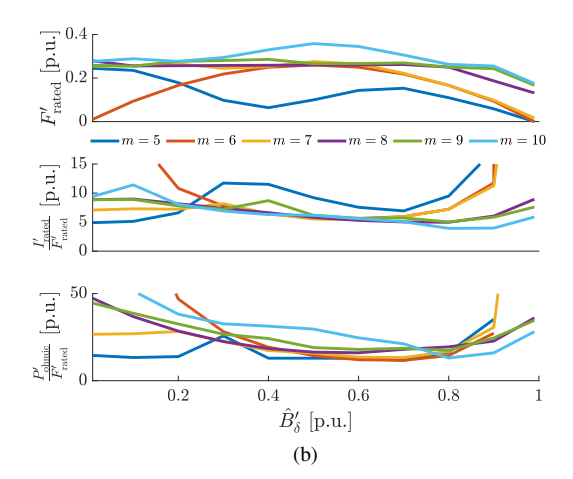
# B. Force Impact on Torque

The machines are also compared in terms of their torque capabilities. In this comparison, the motor creates a constant force (equal to the rotor weight  $W_r$  or its multiple) and the torque that the motor can create at any force angle without exceeding the maximum airgap field limit is determined. Figure 4c presents the results that compare the torque capability of different phases for different magnetizing fields and forces. This plot shows that the torque performance of the m=5 machine is poorer compared to other phases for higher force requirements. For other phases, the torque performance look same with a peak torque identified at  $\hat{B}_{\delta}' = 0.7$  p.u.

# C. Discussion

The findings using the proposed model show that the control of multiple airgap harmonic fields can help enhance the performance of bearingless machines. By controlling four airgap harmonic fields as opposed to two (m=10 vs. m=6 phases), the results reveal that an increase in force rating by over 40% can be achieved at the magnetizing field  $\hat{B}'_{\delta}=0.5$  p.u. This corresponds to an increase in force capacity (33) from 10.4 to 14.3 N/cm² when  $B_{\rm max}=0.8$  T. Similarly, at  $\hat{B}'_{\delta}=0.7$  p.u., controlling four harmonic fields instead of two improves force rating by 36%, increasing the force capacity from 8.7 to 12.2





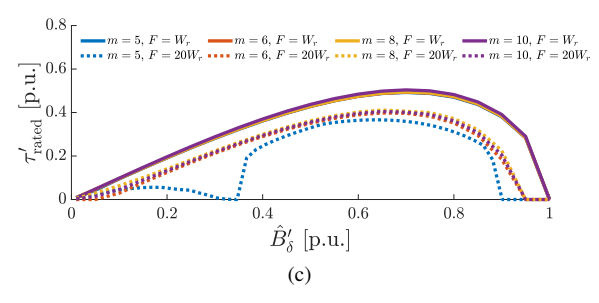


Fig. 4. Comparison between bearingless machines with different phases: (a) maximum force profiles shown for different magnetizing fields, (b) force rating, current rating, and average ohmic losses vs.  $\hat{B}'_{\delta}$ , and (c) torque rating vs.  $\hat{B}'_{\delta}$  for different force magnitudes.

N/cm² for  $B_{\rm max}=0.8$  T. This improvement is advantageous when a bearingless machine operates near iron saturation or requires a large amount of force. Furthermore, designs that support a wide range of magnetizing fields ( $m\geq 8$ ) offer more flexibility during the design stage to meet motor design specifications and during operation to support optimal motor control via field weakening. It is also seen the machines that obtain the maximum torque and force capabilities have  $m\geq 8$  and  $\hat{B}'_{\delta}=0.7$  p.u. These results suggest that the designs with at least three controllable airgap harmonic fields and  $\hat{B}'_{\delta}\approx 0.5$ -0.7 p.u. can be a potential solution to improve bearingless motor performance.

# VI. THEORY VALIDATION

This section provides experimental and FEA validation of the developed theory using a 10-phase bearingless induction motor prototype, shown in Fig. 5a. Section VI-A provides the prototype and test stand description used for the measurements. Sections VI-B and VI-C present hardware mea-

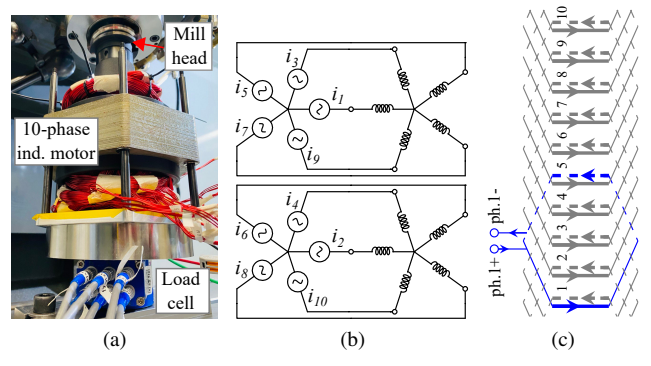


Fig. 5. Ten-phase bearingless induction machine: (a) test setup, (b) drive connections, and (c) winding layout (shown for phase 1).

TABLE I
INDUCTION MACHINE PROTOTYPE PARAMETERS

Stator slots Q	10	Rotor slots $Q_r$	16
Rated torque	1.57 Nm	Rated current	10 Arms
Rated speed	29.5 kRPM	Rated slip	8 Hz
$I_{s_1, \text{rated}}$	8.6 Arms	$I_{s_2, \text{rated}}$	1.4 Arms
$I_{d, \text{rated}}$	6.35 Arms	$I_{s_2,FRW\approx 1}$	0.6 Arms
Experimentally measured:		$k_f$ (at $I_{d, rated}$ )	18.6 N/A
$k_{h_{12}}$	$2.07 \text{ N/A}^2$	$k_{h_{23}}, k_{h_{34}}$	$0.43 \text{ N/A}^2$

surement results that validate the proposed force vector model (Section IV) and demonstrate force enhancement capability (Section V). Section VI-C also provides FEA results that validate force capacity increase under iron saturation.

# A. Prototype and Test Stand Description

The test stand shown in Fig. 5a is used for Sections VI-B and VI-C measurements. The setup consists of the 10-phase induction motor and the drive, a load cell [21], and fixtures to support the stator and the rotor, all mounted within a mill.

The stator winding was designed as a 10-phase combined winding using the methodology of [9], resulting in the winding layout shown in Fig. 5c. Key motor parameters are summarized in Table I. This winding is designed to independently create four airgap space harmonic fields of orders h=1 to 4 with current sequences s=1 to 4, as described in (12). Sequence 1 (p=1) is used to create torque, while three other sequences are used to create suspension forces. The motor phases are connected to the drive terminals in a double five-phase configuration, shown in Fig. 5b. The rotor is a pole-specific squirrel cage rotor designed to have no induced bar currents from  $h=p_s=2$  and its integer multiples [22].

In the following tests, the motor is excited by the phase currents described in (7)-(8). These currents are expected to create the fields described by (13), creating the force:

$$\vec{F}_{10\text{-ph}} = Fe^{j\phi} = \bar{k}_{h_{13}} \vec{i}_1^* \vec{i}_2 + \bar{k}_{h_{23}} \vec{i}_2^* \vec{i}_3 + \bar{k}_{h_{34}} \vec{i}_3^* \vec{i}_4$$
 (34)

Reaction torque and forces acting on the stator are measured using the load cell [21], which is fixed to the mill's X-Y table. The rotor is supported by the mill's spindle and locked at magnetic center. For the measurements in Section VI-C, the radial airgap field is measured in front of each stator tooth using a hall probe [23].

# B. Validation of the Proposed Model

This section presents experimental results that validate the multiharmonic bearingless machine model proposed in Section IV. This is done by exciting the stator winding with different combinations of current sequences and measuring the resulting forces on the rotor. Results are provided in Fig. 6 and 7a-7b

1) Force vector relationship to current sequences: This test is conducted to confirm the first result of Section IV-A, that all combinations of adjacent current sequences create controllable forces. In each test, two sequences  $s_i$  and  $s_j = s_i + 1$  are applied at a low frequency (no torque) and the average forces are measured. The results are used to validate the relationship between forces and current sequences given in (24).

First, measurements are conducted to find the  $\bar{k}_{h_{ij}}$  values in (34). The phase angles  $\phi_{s_i/s_j}$  are set to create force at  $\phi=0$  degrees,  $\hat{I}_{s_i}$  is held constant, and forces are measured for various values of  $\hat{I}_{s_j}$ . Figure 6a subplot 1 presents the measured force vs. sequence 2 current for different sequence 1 currents. Figure 6a subplot 2 shows similar force measurements for sequences 2-3 and 3-4. The slopes of these lines (shown in Fig. 6a) are used to calculate  $k_f$  and  $k_{h_{ij}}$  values, provided in Table I.

Second, measurements are conducted to confirm that each pair of adjacent current sequences can create force at any angle. Magnitudes  $\hat{I}_{s_i/s_j}$  are held constant and the force is measured against  $\Delta\phi_{s_{ij}}=\phi_{s_j}-\phi_{s_i}$ , which is expected to control the force angle based on (24). Figure 6b (column 1) presents the measured force vs.  $\Delta\phi_{s_{12}}$  when  $I_{s_2}=0.6$  Arms. Similarly, Fig. 6b (column 2) shows the results for sequences 2-3 and 3-4. These results confirm that a constant magnitude force vector can be created at any angle using sequence pairs 1-2, 2-3, and 3-4.

- 2) Forces from non-adjacent sequences: The goal of this test is to confirm Section IV-A's finding that non-adjacent current sequences  $s_j \neq s_i \pm 1$  do not contribute to radial force creation. All non-adjacent sequence combinations are tested (1-3, 1-4, and 2-4). In each combination, each current sequence magnitude is set to 5 Arms and the force is measured with respect to the difference in phase angles  $\Delta \phi_{s_{ij}}$ . Figure 7a presents the test results, which confirm that negligible force is created by non-adjacent sequences: the maximum non-zero force observed is 2.83 N, comprising 2.7% of the force created when  $I_{s_1} = I_{s_2} = 5$  Arms.
- 3) Forces from multiple sequences: This test is conducted to validate that the superposition of multiple force vectors created by multiple current sequences matches (29). For each set of currents, the "calculated" force vector is determined by using the  $k_{h_{ij}}$  values found in Section VI-B1 in (34). Figure 7b shows the test results for four different current sequence combinations. The three components of the calculated force vector in (34) are also shown. These results demonstrate the accuracy of the proposed force vector model. The largest differences between the experimental and calculated force vectors are 16% in force magnitude and 5.9° in force angle, indicating a strong correlation between the experimental data and the model.

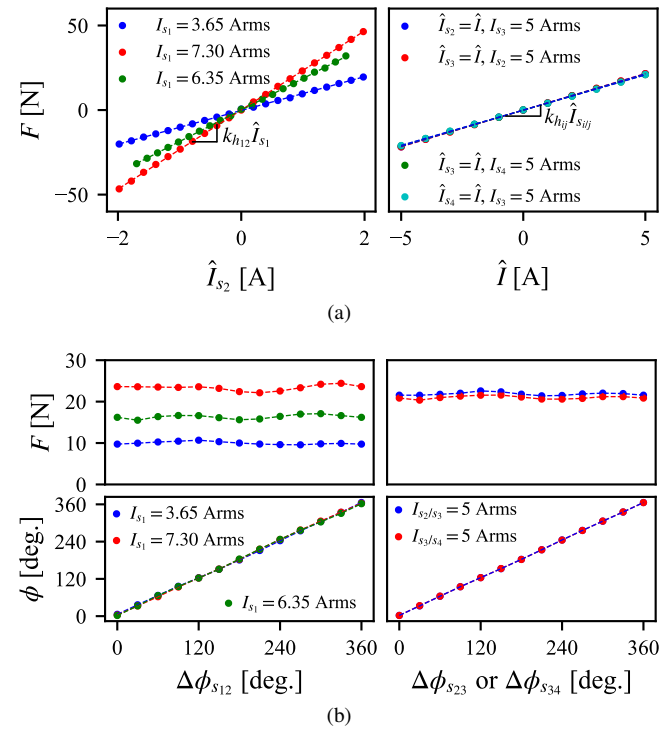


Fig. 6. Experiment results for the validation of the proposed model: forces vs. (a) current magnitudes and (b) current phase angles due to adjacent current sequences.

#### C. Force Enhancement

This section presents test results that validate force enhancement results of Section V. Results of force enhancement within a maximum airgap field limit and transient force response under variable magnetization are presented. Furthermore, force enhancement under iron saturation is demonstrated using FEA. The results are summarized in Fig. 7c-7e and 8.

1) Force enhancement within a maximum airgap field limit: This test demonstrates the force enhancement discussion of Section V. Current sequences 1-2-4 are used to achieve increase in force capacity, as explained in Appendix B. Measurement results presented in Fig. 7c show that sequence 4 can be used to increase force capacity. At  $B_{\rm max}=0.83$  T, force enhancement by approximately 38% is achieved when  $\hat{I}_{s_4}=8$  A, validating the improvement theorized in Section V-C. The fields in front of the stator teeth are also measured to ensure that the airgap field is below  $B_{\rm max}=0.83$  T; measurements are shown in Fig. 7d with dotted markers, while dashed lines represent magnetic fields estimated analytically using (13). This plot confirms that the peak airgap field is below  $B_{\rm max}$  before (red curve) and after (green and cyan curves) force enhancement.

2) Transient force response: This test is conducted to validate force creation that is independent of the magnetization state of the motor. Test results are plotted in Fig. 8, which compares two cases when the force is created by sequences 1-2 (column 1) and 3-4 (column 2). In both cases, a series of step commands is applied to the magnetizing current  $i_d$  to observe its impact on the forces. As shown in Fig. 8 (column 1), the change in the magnetizing current directly impacts the

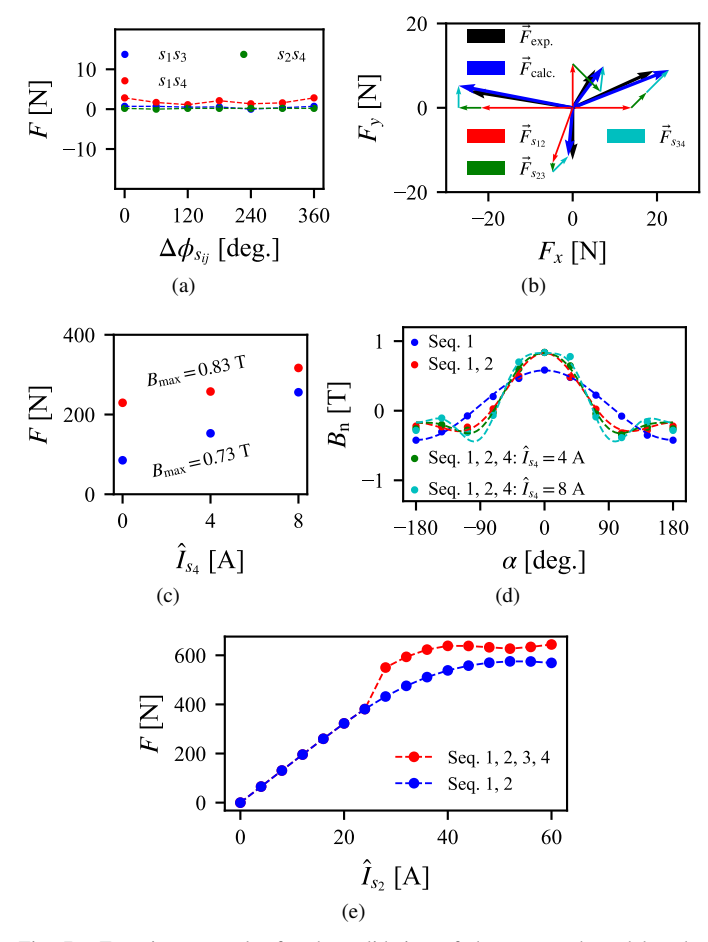


Fig. 7. Experiment results for the validation of the proposed model and force enhancement: (a) forces from non-adjacent sequences, (b) comparison between measured and calculated force vectors at four different points, (c) experiment results of force enhancement using sequence 4 for field weakening, (d) measured airgap magnetic fields corresponding to the  $B_{\rm max}=0.83~{\rm T}$  case of Fig. 7c, and (e) FEA results of force enhancement under iron saturation.

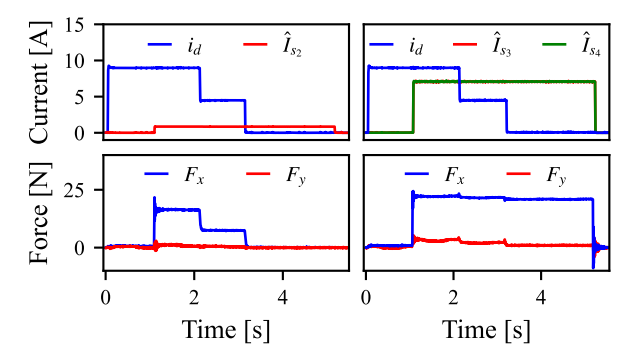


Fig. 8. Measured transient force response using sequences 1-2 and 3-4 under different  $i_d$  magnetizing currents.

force creation. This is because  $i_d$  in this motor is created by sequence 1. The results for case 2 (column 2) show that the force created from sequences 3-4 is approximately constant regardless of the change in  $i_d$ . This is expected based on (34) because sequence 2 is zero and  $i_d$  does not affect the force. These findings demonstrate the potential for enhancing bearingless motor performance under variable magnetization.

3) Force enhancement at iron saturation: An FEA study is conducted to demonstrate force enhancement under iron saturation. This is done in FEA, not hardware, because the high current levels needed to substantially saturate the machine exceeded the capability of the available drive. The results are shown in Fig. 7e. First, the force capability from only sequences 1-2 is found. Sequence 1 is held at  $I_{d,rated}$  and the force is extracted for various  $I_{s_2}$  values. The result (blue curve) shows that increasing  $I_{s_2} \ge 28$  A decreases force creation capability as the iron starts saturating at  $B_{\text{max}} \approx 1.03 \text{ T. Second}$ , sequences 3 and 4 are additionally injected to enhance the force for  $I_{s_2} \ge 28$  A. These currents are calculated following the steps from Section V-A with  $B_{\rm max} \approx 1.03~{\rm T}$  and loaded into the FEA model. The result (red curve) demonstrates the potential for force enhancement using sequences 3 and 4. At  $\hat{I}_{s_2} \approx 28$  A, the maximum force enhancement (27%) is observed.

#### VII. CONCLUSION

This paper proposes a multiharmonic model for bearingless electric machines using current space vector/sequence components and their relationship to airgap magnetic field space harmonics. It is found that previous attempts at developing precise models for magnetic bearings and bearingless motors can be viewed as special cases of the generalized model developed in this paper. Furthermore, the paper finds that all three-phase combined windings and some three-phase separated windings have force vector components with quadratic relationship to current space vectors, which have been neglected in previous literature. The paper shows that when these terms are ignored in the force model, substantial force vector error can result; however, when properly handled, these additional forces can increase the machine's force rating.

The proposed model is applicable to all motor types, is analytic-based, and captures the underlying physics of the machine accurately. These features equip machine and controls designers with tools to increase the torque and levitation system performance. The paper shows that the developed model can be used to eliminate the force vector error by selecting certain combinations of machine parameters during the design stage or by having the control system analytically solve the proposed model during runtime to determine phase currents as the sum of multiple current sequences. The paper further shows that by using the proposed model to actuate more than two harmonics, either force creation can be decoupled from the motor's magnetization state or force capacity can be substantially increased. A 40% force capacity increase over the standard approach to bearingless motors is demonstrated for machines that control four airgap harmonics. Experimental results from a prototype 10-phase induction machine validate the proposed model and increased force capacity.

In conclusion, the findings of this paper motivate rethinking the design approach of bearingless machines to include additional force creation mechanisms and to develop regulation techniques that use the proposed model. These developments can make the design space of bearingless machines less constrained and close the performance gap between bearingless machines and the best motors and magnetic bearings.

# APPENDIX A DIMENSIONLESS FORCE VECTOR MODEL

This paper (Section V) makes use of the p.u. force vector model to find the force capacity in bearingless machines. The model is expressed in terms of the p.u. radial field quantities, which are normalized by a maximum allowable airgap field  $B_{\text{max}}$ . By setting the base value  $F_{\text{b}} = \frac{V_r}{2\mu_0 r} B_{\text{max}}^2$  in (19), it can be shown that (29)-(30) can be expressed in a p.u. form as

$$\vec{F}' = \sum_{i=1}^{n_f} C_{h_{ij}} \hat{B}'_{\mathsf{n},h_i} \hat{B}'_{\mathsf{n},h_j} e^{j(\phi_{s_j} - \phi_{s_i})}$$
(35)

where  $h_j = h_i + 1$ ,  $n_f$  is the total number of force vectors, and  $\hat{B}'_{\mathbf{n},h_{i,j,k}}$  is a p.u. radial field amplitude.

The base values for currents, ohmic losses, and torque that are used in Section V are given by

$$I_{\rm b} = \frac{\pi \delta_{\rm eff}}{\mu_0 m z_Q z_c B_{\rm max}}, \ P_{\rm b} = I_{\rm b}^2 R_{\rm ph} m, \ \tau_{\rm b} = \frac{V_r p \delta_{\rm eff}}{\mu_0 r} B_{\rm max}^2$$
(36)

Note that these base values are same for all designs compared in Section V, which allows comparing them in p.u.  $I_b$  is set using (14), resulting in the p.u. relationship between current and field quantities as  $\hat{I}'_s = h\hat{B}'_{n,h}/\hat{k}_{w,h}$ .  $P_b$  is set based on its relationship to currents;  $\tau_b$  is set using (21), resulting in the p.u. equation for torque  $\tau' = \hat{B}'_\delta \hat{B}'_{n,w,p}$ . Note that, if machines with various pole pairs are being compared, the torque base value  $\tau_b$  in (36) needs to be adjusted not to have p, resulting in the p.u. torque equation of  $\tau' = p\hat{B}'_\delta \hat{B}'_{n,w,p}$ .

#### APPENDIX B

# FIELDS AND CURRENTS FOR INCREASED FORCE CAPACITY

This appendix summarizes the approach created for this paper to calculate magnetic fields and currents that maximize the force rating of a 10-phase bearingless machine. The approach is based on numerical calculations from Section V-A and uses sequence 4 for flux weakening, enabling sequences 1 and 2 to generate larger force for a given maximum airgap field. This approach can be directly implemented in a controller without requiring complex lookup tables.

Table II provides estimations for optimal field magnitudes and angles derived from numerical calculations for magnetizing fields  $\hat{B}'_{\delta} \approx 0.5\text{-}0.7$  p.u. Based on the desired force requirement  $F'^* = \hat{B}'_{\delta}\hat{B}'_{\mathrm{n},h_2}$ , if  $\hat{B}'_{\mathrm{n},h_2} \leq 1 - \hat{B}'_{\delta}$  (column 2), there is no need to excite sequence 4, as the total airgap field remains below the maximum limit of 1 p.u. For a larger force requirement with  $\hat{B}'_{\mathrm{n},h_2} > 1 - \hat{B}'_{\delta}$ ,  $\hat{B}'_{\mathrm{n},h_2}$  can be increased up to  $1.2 - \hat{B}'_{\delta}$  (column 3) and harmonic 4 can be actuated according to Table II, ensuring that the airgap field remains within 1 p.u. Using these optimal fields, the required current sequences for phase k are computed using (8). This requires knowledge of the tesla per ampere parameter for each harmonic-sequence pair, which can be calculated using (14), FEA simulations, or measurements.

 $TABLE \; II \\ Optimal \; Fields \; for \; Max. \; Force \; Rating \; with \; Seq. \; 1-2 \; vs. \; 1-2-4. \\$ 

	Sequences 1-2	Sequences 1-2-4
$\hat{B}'_{n,h_2}, \phi_{s_2}$	$\leq 1 - \hat{B}'_{\delta},  \theta + \phi$	$\leq 1.2 - \hat{B}_{\delta}',  \theta + \phi$
$\hat{B}'_{n,h_4},\phi_{s_4}$	NA	$\hat{B}'_{\delta} + \hat{B}'_{n,h_2} - 1,  \pi + 3\theta + \phi$

#### REFERENCES

- A. Chiba, T. Fukao, O. Ichikawa, M. Oshima, M. Takemoto, and D. Dorrell, Magnetic Bearings and Bearingless Drives. Newnes, 2005.
- [2] J. Chen, J. Zhu, and E. L. Severson, "Review of bearingless motor technology for significant power applications," *IEEE Transactions on Industry Applications*, vol. 56, no. 2, pp. 1377–1388, 2020.
- [3] G. Sala, G. Valente, A. Formentini, L. Papini, D. Gerada, P. Zanchetta, A. Tani, and C. Gerada, "Space vectors and pseudoinverse matrix methods for the radial force control in bearingless multisector permanent magnet machines," *IEEE Transactions on Industrial Electronics*, vol. 65, no. 9, pp. 6912–6922, Sep. 2018.
- [4] G. Munteanu, A. Binder, and T. Schneider, "Loss measurement of a 40 kw high-speed bearingless pm synchronous motor," in 2011 IEEE Energy Conversion Congress and Exposition, 2011, pp. 722–729.
- [5] N. R. Hemenway and E. L. Severson, "Three-pole magnetic bearing design and actuation," *IEEE Transactions on Industry Applications*, vol. 56, no. 6, pp. 6348–6359, 2020.
- [6] N. Turk, N. Bulić, and W. Gruber, "Nonlinear control of a bearingless flux-switching slice motor with combined winding system," *IEEE/ASME Transactions on Mechatronics*, vol. 25, no. 1, pp. 152–163, 2020.
- [7] S. M. Mirić, R. V. Giuffrida, D. Bortis, and J. W. Kolar, "Enhanced complex space vector modeling and control system design of multiphase magnetically levitated rotary–linear machines," *IEEE Journal of Emerging and Selected Topics in Power Electronics*, vol. 8, no. 2, pp. 1833–1849, 2020.
- [8] A. Khamitov and E. L. Severson, "Exact torque and force model of bearingless electric machines," in 2022 IEEE Energy Conversion Congress and Exposition (ECCE). IEEE, 2022, pp. 1–8.
- [9] F. Nishanth, A. Khamitov, and E. L. Severson, "Design of electric machine windings to independently control multiple airgap harmonics," *IEEE Transactions on Industry Applications*, pp. 1–12, 2023.
- [10] J. Pyrhonen, T. Jokinen, and V. Hrabovcova, Design of rotating electrical machines. John Wiley & Sons, 2013.
- [11] T. A. Lipo, Analysis of synchronous machines. Crc Press, 2017.
- [12] A. Khamitov and E. L. Severson, "Design of multi-phase combined windings for bearingless machines," *IEEE Transactions on Industry Applications*, vol. 59, no. 3, pp. 3243–3255, 2023.
- [13] A. Wilamowski and M. Bogdan, "The industrial electronics handbook power electronics," *Taylor and Francis Group*, 2011.
- [14] G. Grandi, G. Serra, and A. Tani, "General analysis of multi-phase systems based on space vector approach," in 2006 12th International Power Electronics and Motion Control Conference. IEEE, 2006, pp. 834–840.
- [15] A. Khamitov, W. Gruber, G. Bramerdorfer, and E. L. Severson, "Comparison of combined winding strategies for radial nonsalient bearingless machines," *IEEE Transactions on Industry Applications*, vol. 57, no. 6, pp. 6856–6869, 2021.
- [16] W. Gruber and S. Silber, "Dual field-oriented control of bearingless motors with combined winding system," in 2018 International Power Electronics Conference (IPEC-Niigata 2018 -ECCE Asia), May 2018, pp. 4028–4033.
- [17] T. Schneider, J. Petersen, and A. Binder, "Influence of pole pair combinations on high-speed bearingless permanent magnet motor," 2008.
- [18] A. Farhan, M. Johnson, K. Hanson, and E. L. Severson, "Design of an ultra-high speed bearingless motor for significant rated power," in 2020 IEEE Energy Conversion Congress and Exposition (ECCE), 2020, pp. 246–253.
- [19] J. Chen, A. Farhan, M. Johnson, and E. L. Severson, "Design of bearingless permanent magnet motors using no voltage combined windings," in *The 10th International Conference on Power Electronics, Machines* and Drives (PEMD 2020), vol. 2020, 2020, pp. 803–808.
- [20] E. H. Maslen, G. Schweitzer, H. Bleuler, and M. Cole, Magnetic bearings: theory, design, and application to rotating machinery. Springer, 2009.

- [21] MCS10, Multicomponent sensor, 2017, vendor: HBM, part number: MCS10-005. [Online]. Available: http://spectromas.ro/wpcontent/uploads/2017/12/Fisa-tehnica-MCS10.pdf
- [22] J. Chen, M. W. Johnson, A. Farhan, Z. Wang, Y. Fujii, and E. L. Severson, "Reduced axial length pole-specific rotor for bearingless induction machines," *IEEE Transactions on Energy Conversion*, vol. 37, no. 4, pp. 2285–2297, 2022.
- [23] AN180KIT for AKM HG-106C-2U Hall Element Y axis, Thin, High Magnetic Field Sensor, 2016, vendor: GMW Associates, part number: HG-106C-2U. [Online]. Available: https://gmw.com/wp-content/uploads/2019/01/AN180KIT-AKM-HG-106C-2U-92716.pdf



Anvar Khamitov (Member, IEEE) received the B.Eng. degree in electrical and electronic engineering from Nazarbayev University, Astana, Kazakhstan, in 2018, and the Ph.D. degree in electrical and computer engineering from the University of Wisconsin-Madison (UW-Madison), USA, in 2024. He is currently an Electromagnetic Application Engineer at Powersys, Madison, USA, where he specializes in the application of JMAG software for the design and analysis of electric machines and electromagnetic systems.

Previously, Anvar was a Research Assistant at the Wisconsin Electric Machines and Power Electronics Consortium (WEMPEC), working with Dr. Severson, where his research focused on the design, modeling, optimization, and control of electric machines, with a particular emphasis on bearingless machines and off-highway vehicle electrification. Anvar's research interests now also include electromagnetic analysis, multi-physics analysis, and the application of electric machines using advanced software tools like JMAG and HPC resources. He is the recipient of the Wisconsin Power Engineering Award from UW-Madison in 2022 and the Student Best Paper Award at the International Symposium on Magnetic Bearings (ISMB) in Lyon, France, in 2023.



**Eric L Severson** (S'09-M'15-SM'22) received the B.Sc. and PhD degrees in electrical engineering from the University of Minnesota, Minneapolis, USA in 2008 and 2015, respectively where he also worked as a post doctoral associate through 2016.

In 2017, Dr. Severson joined the Electrical and Computer Engineering faculty at the University of Wisconsin-Madison, where he received tenure and was an associate director of the Wisconsin Electric Machines and Power Electronics Consortium (WEMPEC) and fellow of the Grainger Institute for

Engineering. In 2023, he joined the University of Minnesota's Mechanical Engineering Department, where he is now Associate Professor. His research interests include design and control of electric machines, with focus areas in bearingless motors, magnetic bearings, torque-dense machinery, off-highway vehicle electrification, and flywheel energy storage.

Dr. Severson is a recipient of the USA National Science Foundation CAREER Award in 2020, the Department of Defense NDSEG fellowship in 2009, and the National Science Foundation Graduate Research Fellowship in 2009.